Supplementary Information

Anisotropic arrayed nano-slots metasurfaces fabrication by reflective plasmonic lens beyond near field optical lithography

Jun Luo,[a,b] Bo Zeng,[a] Changtao Wang,[a] Ping Gao,[a] Kaipeng Liu, [a] Mingbo Pu,[a] Jinjin Jin,[a] Zeyu Zhao,[a] Xiong Li, [a] Honglin Yu,[b] and Xiangang Luo * [a]

[a.] *State Key Laboratory of Optical Technologies on Nano-Fabrication and Micro-Engineering, Institute of Optics and Electronics, Chinese Academy of Science, P.O. Box 350, Chengdu 610209, China.*

[b.] *Key Laboratory of Optoelectronic Technology and System, Ministry of Education, Chongqing University, Chongqing 400030, China.*

** Email address: lxg@ioe.ac.cn*

1. The permittivities obtained by the spectroscopic ellipsometry (SE850)

The permittivities are obtained by the spectroscopic ellipsometry (SE850). The following Table. S1 shows the experimental parameters for determination the permittivities of Cr, PR and Ag.

Table. S1 Measurement the perimittivities with ellipsometry

Spectroscopic ellipsometry (SE850 SENTECH)						
Material	Thickness	Substrate	Process of coating fillm	Incident angle	Mode-based analysis	Primittivity(365nm)
Cr	40 nm	Si	Magnetron sputtering	70°	Drude-Lorentz	-8.55+8.96i
PR	30 nm	Si	Spin-coating	70°	Cauchy dispersion	2.59
Ag	20 nm	Si	Evaporation	70°	Tauc-Lorentz	-2.168+0.358i

2. Optimizing the thickness of film

The thicknesses of Cr, PR and Ag are mainly determined by considering both the calculated imaging property and the convenience of structure fabrication, pattern transfer process. In theory, reflective imaging with sub-diffraction resolution usually occurs as the permittivity of Ag matches that of resist layer at the used light wavelength. But the imaging property would be greatly affected by the thickness of the films. To show this point, the Fig. S1 presents the imaging field dependence on the variant thickness of Cr, PR and Ag film, for 50nm width dense lines pattern with L/S =1:1. For instance, PR with thickness 20 nm shows better imaging contrast than that of 30 nm, due to the enhanced excitation of surface plasmon in this case. But this would result in the difficulty of pattern transfer from PR to Ag with small PR thickness. So we choose 30 nm thickness of PR. Similar problems lies in the design of Cr and Ag films (Fig. S1b and S1d). Usually, Ag and Cr must be thick enough, at least larger than the skin depth, to block light transmission and help to get high contrast imaging. On the other hand, the FIB milling and IBE etching process require thin films. So 40 nm Cr and 50 nm Ag are employed in our experiments.

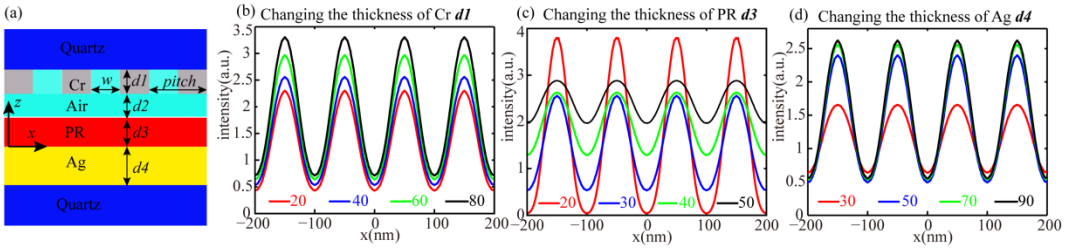

Fig.S1 (a) The schematic of plasmonic litghography structure for determining the thickness of Cr, PR and Ag, *pitch*=100 nm, *w*=50 nm, the thickness of air *d2*=10 nm. The simulated results are performed by the finite element method with Comsol Mulitphysics 4.3. (b) The intensity distributions at *d3*/2 above the reflective Ag -PR interface for TM polarization light illumination when changing the thickness of *d1* (*d3=30* nm, *d4=50 nm*). (c) The intensity distributions for changing the thickness of *d3* (*d1=40* nm, *d4=50 nm*). (d) The intensity distributions for changing the thickness of *d4* (*d1=40* nm, *d3=30 nm*).

Further, we can also make some theoretical analysis as described by an optical transmission function of imaging model for planar plasmonic lens in the following form.[1]

$$\begin{bmatrix} E_x(x,y,z) \\ E_y(x,y,z) \\ E_z(x,y,z) \end{bmatrix} = \int_{-\infty}^{\infty}\int_{-\infty}^{\infty} \begin{bmatrix} A_x(k_x,k_y) \\ A_y(k_x,k_y) \\ \dfrac{k_x A_x + k_y A_y}{-k_z} \end{bmatrix} \times \exp(ik_x x + ik_y y)dk_x dk_y ,$$

and

$$\begin{bmatrix} A_x(k_x,k_y) \\ A_y(k_x,k_y) \end{bmatrix} = \int_{-\infty}^{\infty}\int_{-\infty}^{\infty} \begin{bmatrix} G_x(x,y)t_x(x,y)T_x(k_x,k_y) \\ G_y(x,y)t_y(x,y)T_y(k_x,k_y) \end{bmatrix} \exp(-ik_x x - ik_y y)dxdy,$$

where $G(x, y)$, $t(x, y)$ and $T(k_x, k_y)$ are the illumination function, transmission function of object and optical transfer function (OTF) of plasmonic lens, respectively. The OTF can be obtained through transfer matrix. In our structure, there is a reflection plane in the plasmonic lens, so the OTF was determined by using the fields in the photoresist layer.

3. The effect of surface topography on the quality of imaging

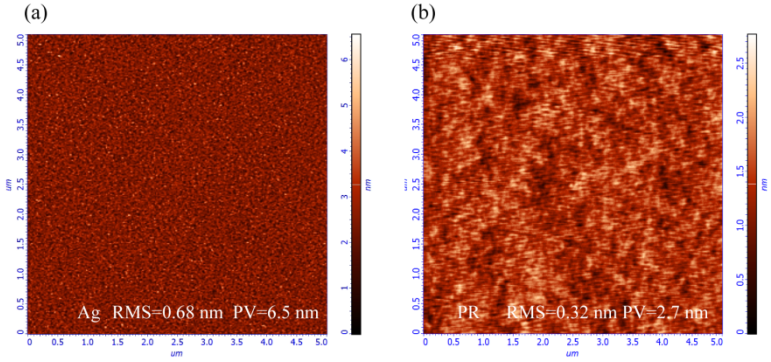

Fig. S2 (a) The AFM measured surface roughness of reflective Ag slab (RMS=0.68 nm, PV=6.5 nm). (b) The AFM measured surface roughness of the PR layer (RMS=0.32 nm, PV=2.7 nm).

In our experiment, the Ag film roughness is reduced to be 0.68 nm with Ge seed method. This help to improve the quality of resist patterns, as could be seen in the Fig. S3. Fig.S3 (b)-(m)

demonstrate that the intensity distributions would be disturbed for larger RMS and PV, and then resulting in line edge roughness and scattering loss. So rough surface topography would perturb the surfaces plasmon modes and increase scattering loss resulting in diminishing resolution. Good imaging quality could be obtained only if the surface topography is well controlled.[2,3]

On the other hand, the topography variation over a large area of mask and substrate is an important issue for large area lithography. This occurs because that the air space variation between pattern and resist would deliver imaging contrast degradation as well as change of image intensity. As could be seen in Fig. 3(c) and 3(d), the air space variation should be smaller than 10 nm or less. To solve this problem, the surface topography of substrate are precisely manufactured even with ion beam polishing, and the measured peak to valley (PV) value is below 30nm over a substrate with 25mm diameter and 5mm thickness. The mask pattern is fabricated on a thin fused silica plate (25mm diameter, ~0.35mm thickness). Thus, with the help of nearly uniform air pressure (~0.3 MPa), the flexibility of mask would allow adaptive topography change and realize close contacting between mask and resist layer. And the air space variation would be small enough to obtain a large lithography pattern. In our experiment, resist patterns (~6μm x 6μm) with 64 nm period dense lines and sparsely located in a ~10mm x 10mm area were successfully tested in lithography.

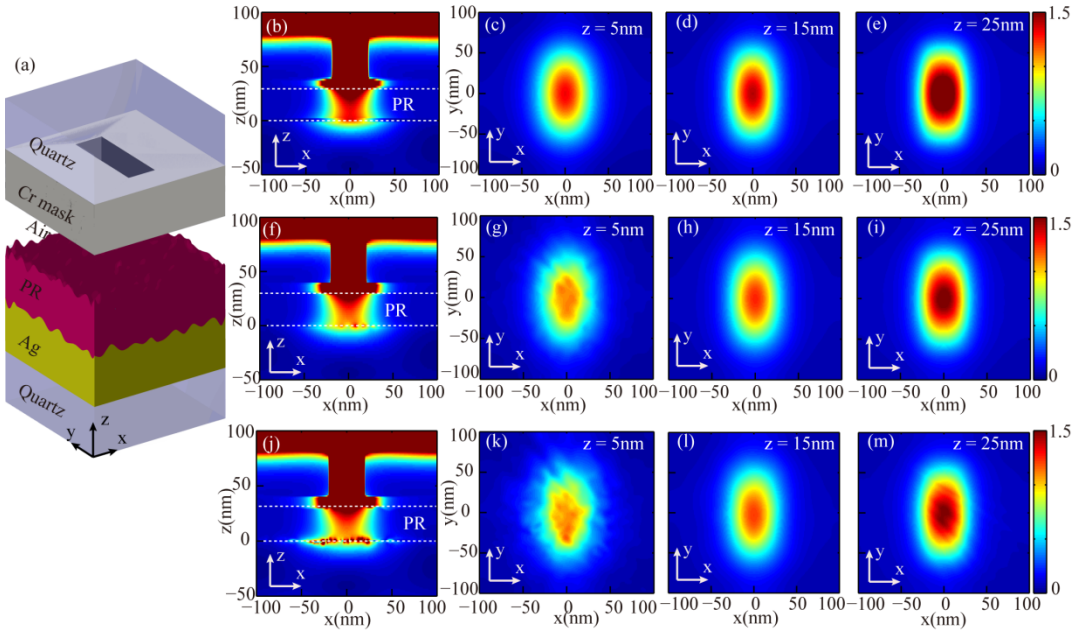

Fig. S3 (a) The schematic of the single nano-slot plasmonic lithography structure with roughness, other parameters are the same with that of in Fig. 1a. The calculated results are performed with periodic boundary condition in FIT simulation. (b)-(e) The electric field intensity distribution in the *xz* (*y* = 0 nm) and xy (z = 5, 15, 25nm) plane for the plamonic lithography structure with smooth surfaces (Ag layer RMS = 0 nm and PV=0, PR layer RMS = 0 nm and PV=0,), respectively. (f)-(i) The simulated results for the plamonic lithography structure with roughness and PV (Ag reflective layer RMS = 0.68 nm and PV=6.5 nm, PR layer RMS = 0.32 nm and PV=2.7 nm), respectively. (j)-(m) The simulated results for the plamonic lithography structure with roughness and PV (Ag reflective layer RMS = 1.9 nm and PV=14nm, PR layer RMS = 2 nm and PV=15nm), respectively.

4. Detail of the Fig. 5b and Fig. 6b

Fig. 5b and Fig. 6b was obtained by means of the iron milling instrument (IM 4000, Hitachi). Prior to milling, the Pt film with a thickness of 35nm was sputtered on the sample by sputtering instrument (E-1045, Hitachi), in order to protect the surface of the photoresist from the iron milling and at the same time reduce charging effects when the specimen was characterized by SEM.

5. The optics principle of anisotropic arrayed nano-slots metasurfaces

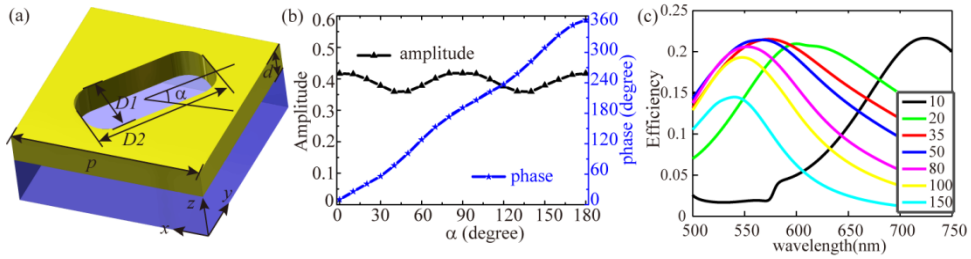

Fig. S4 (a) A unit cell with the size of *D1* = 75nm, *D2* = 150nm, the periodic of unit cell *p*=200nm, and the thickness of silver *d* =50 nm, and *α* is the angle between the major axes of nano-slot and the *x* axis direction. (b) The amplitude and phase of cross-polarization transmission light vary with the angle of α for the circular polarization light illumination at 633nm wavelength. The relationship between the phase of cross-polarization transmission light β and the rotating angle α is β ≈ 2α. (c) The cross-polarization transmission efficiency vs the thickness of Ag.

According to the generalized Snell law,[4-8] the phase shift, range from 0 to 2π, can be realized by varying the geometry parameters of nano-antennas or nano-voids. We apply the generalized Snell law to design anisotropic arrayed nano-slots metasurfaces. The nano-slot aperture could convert the circularly polarized (CP) light to the cross-polarization with opposite handedness, and the phase shift of cross-polarization would cover the whole [0, 2π] by rotating the major axis of nano-slot. The amplitude and phase of cross-polarization transmission light varying with the rotating angle of the nano-slot is plotted Fig. S4 when the unit cell is illuminated with circular polarization light at 633nm wavelength. To obtain a convergent wavefronts, the nano-slots are arrayed with parabolic phase distribution by rotating the major axis of nano-slots. The relationships between the phase distribution of nano-slot φ and its location central coordinate *x* and *y* are described as below:

$$\varphi(x,y) = \frac{2\pi}{\lambda}\left(\sqrt{x^2 + y^2 + f^2} - f\right)$$

where λ is the wavelength of incident light and *f* is the focal length(*f* = 3 μm).

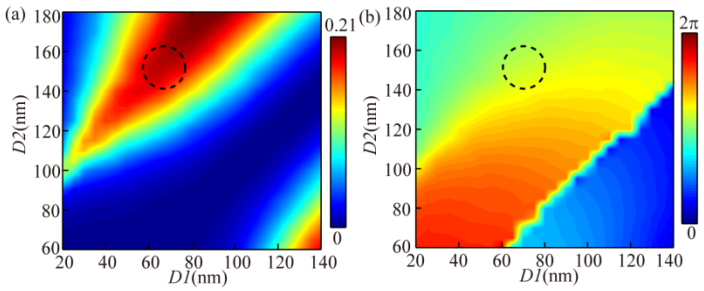

Fig. S5 The transmittance and phase of cross-polarization light at 633nm wavelength varying with the size of *D1* and *D2* are plotted in (a) and (b) by sweeping the parameters of unit cell, and the unit cell is shown in Fig. S3(a). The area of black dash curve represents the size of *D1* and *D2* of fabricated nano-slots.

We plot the transmittance and phase of cross-polarization light as a function of the size of *D1* and *D2* for circular polarization illumination at 633 nm wavelength as shown in Fig.S5. The area of black dash curve represents the size of *D1* and *D2* of fabricated nano-slots. Size errors with ±10 nm would result in ~3% deviation of efficiency and ~20° deviation of phase. These deviations could lead to the differences between the experiment and the simulation.

6. Measured the optical property of fabricated metalens with about 35nm thickness at 633nm and 532nm wavelength

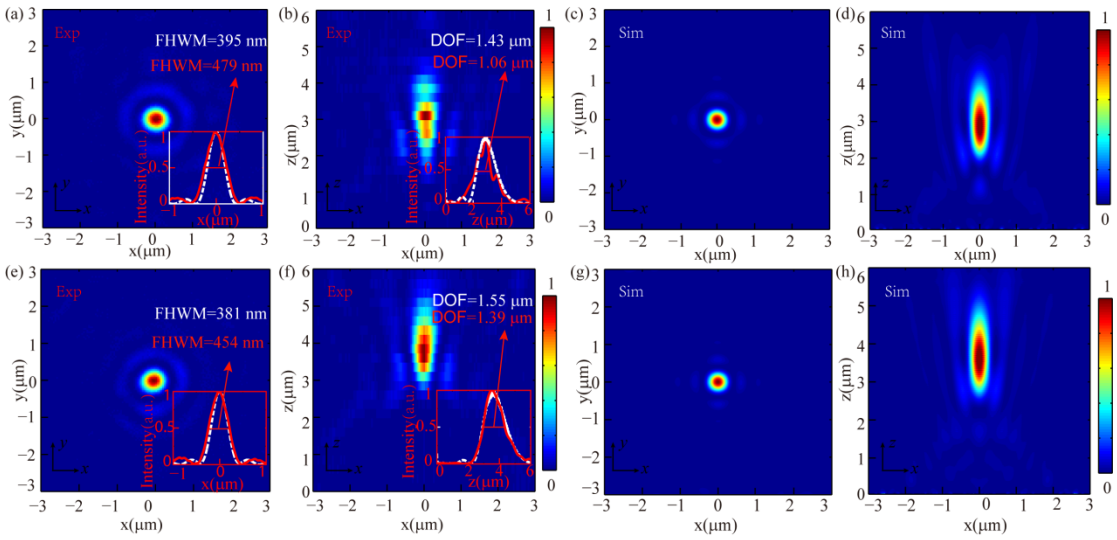

Fig. S6 (a) - (d) The cross sections intensity distributions for the circularly polarized light with 633nm wavelength, Experimental intensity distributions in the *xy* plane (a) and in the *xz* plane (b), simulated intensity distributions in the *xy* plane (c) and in the *xz* plane (d). The inset maps in (a) and (b) show intensity distributions along the *x*-axis and *z*-axis. The white and red curves represent the simulated and experimental of the metalens, respectively. (e)-(h) The cross sections intensity distribution for the circularly polarized light with 532nm wavelength, Experimental intensity distributions in the *xy* plane (e) and in the *xz* plane (f), simulated intensity distributions in the *xy* plane (g) and in the *xz* plane (h).

We also measured the focusing property of fabricated metalens with 35nm thickness for circularly polarized incident light with 633nm and 532 nm wavelength as shown in Fig.S6. The experimental and simulated results for the circularly polarized light illumination with 633 nm wavelength are illustrated in Fig. S6 (a) - (d). The full widths at half maximum (FWHM) of measurement and simulation are 479 nm and 395 nm. The depth of focus (DOF) of measurement and simulation are 1.06 μm and 1.43 μm, respectively. The focusing efficiencies for 633 nm are about 8% (efficiency of the simulation is 14.2%). For the circularly polarized incident light with 532 nm wavelength, the results of measurement and simulation are shown in Fig. S6 (e)-(h). The FWHM of measurement and simulation are 454nm and 381nm, and the DOF of measurement and simulation are 1.39 μm and 1.55μm, respectively. The efficiency is about 3% (efficiency of the simulation is 7.3%).

The focusing efficiency at 532 nm is lower than that at 633 nm, which could mainly attribute to the more loss in the high frequency region.

References

1 X. Luo, Science China Physics, Mechanics & Astronomy, 2015, **58**, 1-18.

2 H. Liu, B. Wang, L. Ke, J. Deng, C. C. Choy, M. S. Zhang, L. Shen, S. A. Maier and J. H. Teng, High contrast superlens lithography engineered by loss reduction. *Adv. Funct. Mater*., 2012, 22, 3777-3783.

3 H. Liu, B. Wang, L. Ke, J. Deng, C. C. Chum, S. L. Teo, L. Shen, S. A. Maier and J. Teng, High aspect subdiffraction-limit photolithography via a silver superlens. *Nano Lett*., 2012, 12, 1549-1554

4 N. Yu, P. Genevet, M. A. Kats, F. Aieta, J.-P. Tetienne, F. Capasso and Z. Gaburro, Light propagation with phase discontinuities: generalized laws of reflection and refraction. *Science*, 2011, 334, 333-337.

5 L. Zhang, J. Hao, M. Qiu, S. Zouhdi, J. K. W. Yang and C.-W. Qiu, Anomalous behavior of nearly-entire visible band manipulated with degenerated image dipole array. *Nanoscale*, 2014, 6, 12303-12309.

6 X. Yin, Z. Ye, J. Rho, Y. Wang and X. Zhang, Photonic spin Hall effect at metasurfaces. *Science*, 2013, 339, 1405-1407.

7 X. Ni, S. Ishii, A. V. Kildishev and V. M. Shalaev, Ultra-thin, planar, Babinet-inverted plasmonic metalenses. *Light. Sci. & Appl.,* 2013, 2, e72.

8 X. Chen, L. Huang, H. Mühlenbernd, G. Li, B. Bai, Q. Tan, G. Jin, C.-W. Qiu, S. Zhang and T. Zentgraf, Dual-polarity plasmonic metalens for visible light. *Nat. Commun*., 2012, 3, 1198.